

1 Frequency, magnitude and character of hyperthermal 2 events at the onset of the Early Eocene Climatic 3 Optimum

4 V. Lauretano¹, K. Littler^{2,*}, M. Polling¹, J. C. Zachos², L. J. Lourens¹

5 [1]{Department of Earth Sciences, Faculty of Geosciences, Utrecht University,
6 Budapestlaan 4, 3584CD, Utrecht, The Netherlands}

7 [2]{ Department of Earth and Planetary Sciences, University of California Santa Cruz,
8 1156 High Street, Santa Cruz, CA 95064, USA}

9 [*]{now at: Camborne School of Mines, University of Exeter, Penryn Campus,
10 Penryn, Cornwall, TR10 9FE, United Kingdom}

11 Correspondence to: Vittoria Lauretano (v.lauretano@uu.nl)

12 13 **Abstract**

14 Recent studies have shown that the Early Eocene Climatic Optimum (EECO) was
15 preceded by a series of short-lived global warming events, known as hyperthermals.
16 Here we present high-resolution benthic stable carbon and oxygen isotope records
17 from ODP Sites 1262 and 1263 (Walvis Ridge, SE Atlantic) between ~54 and ~52
18 million years ago, tightly constraining the character, timing, and magnitude of six
19 prominent hyperthermal events. These events, which include Eocene Thermal
20 Maximum (ETM) 2 and 3, are studied in relation to orbital forcing and long-term
21 trends. Our findings reveal an almost linear relationship between $\delta^{13}\text{C}$ and $\delta^{18}\text{O}$ for all
22 these hyperthermals, indicating that the eccentricity-paced co-variance between deep-
23 sea temperature changes and extreme perturbations in the exogenic carbon pool
24 persisted during these events towards the onset of the EECO, in accord with previous
25 observations for the Paleocene Eocene Thermal Maximum (PETM) and ETM2. The
26 covariance of $\delta^{13}\text{C}$ and $\delta^{18}\text{O}$ during H2 and I2, which are the second pulses of the
27 “paired” hyperthermal events ETM2-H2 and I1-I2, deviates with respect to the other
28 events. We hypothesize that this could relate to a relatively higher contribution of an

29 isotopically heavier source of carbon, such as peat or permafrost, and/or to climate
30 feedbacks/local changes in circulation. Finally, the $\delta^{18}\text{O}$ records of the two sites show
31 a systematic offset with on average 0.2‰ heavier values for the shallower Site 1263,
32 which we link to a slightly heavier isotopic composition of the intermediate water
33 mass reaching the northeastern flank of the Walvis Ridge compared to that of the
34 deeper northwestern water mass at Site 1262.

35

36 **1 Introduction**

37 The early Paleogene was characterized by a highly dynamic climatic system both on
38 long- ($>10^6$ years) and short- ($<10^4$ years) time scales. From the late Paleocene (~ 58
39 Ma) to the early Eocene (~ 50 Ma), Earth's surface experienced a long-term warming
40 trend that culminated in an extended period of extreme warmth, called the Early
41 Eocene Climatic Optimum (EECO; Zachos et al., 2001, 2008; Bijl et al., 2009;
42 Westerhold and Röhl, 2009). During the EECO, global temperatures reached a long-
43 term maximum lasting about 2 Myr, characterized by the warmest temperatures of the
44 Cenozoic (Zachos et al., 2008). Superimposed on the long-term warming trend were a
45 series of short-lived global warming (hyperthermal) events, accompanied by the
46 release of ^{13}C -depleted carbon into the ocean-atmosphere carbon reservoirs (Zachos et
47 al., 2005; Lourens et al., 2005; Nicolo et al., 2007; Littler et al., 2014; Kirtland Turner
48 et al., 2014). These events are of particular interest as they represent useful analogs
49 for the current global warming, despite differences in background climatic conditions
50 and rates of change (e.g., Zachos et al., 2008; Hönisch et al., 2012; Zeebe and Zachos,
51 2013).

52 The Paleocene Eocene Thermal Maximum (PETM or ETM1, ~ 56 Ma), lasting less
53 than 200 kyr, was the most extreme of these episodes. During the PETM global
54 temperature rose by $5\text{--}8^\circ\text{C}$, and massive amounts of carbon were released as
55 evidenced by a significant negative carbon isotope excursion (CIE) of $>3\text{‰}$ in the
56 ocean/atmosphere carbon pools, and widespread dissolution of seafloor carbonate
57 (Kennett and Stott, 1991; Dickens et al., 1995; Thomas and Shackleton, 1996; Zachos
58 et al., 2005; Sluijs et al., 2007; Zachos et al., 2008; McInerney and Wing, 2011). A
59 series of similar events are recorded in carbonate records from marine and continental
60 deposits from the early Paleogene, as expressed by negative excursions in $\delta^{13}\text{C}$ and
61 $\delta^{18}\text{O}$ often accompanied by dissolution horizons (e.g., Cramer et al., 2003; Lourens et

62 al., 2005; Agnini et al., 2009; Galeotti et al., 2010; Stap et al., 2010; Zachos et al.,
63 2010; Abels et al., 2012; Slotnick et al., 2012; Kirtland Turner et al., 2014; Littler et
64 al., 2014; Abels et al., 2015). Orbitally tuned records for this geological interval
65 provide evidence that the early Eocene hyperthermal events were paced by variations
66 in the Earth's orbit, specifically in the long- and short- eccentricity cycles. (e.g.,
67 Cramer et al., 2003; Lourens et al., 2005; Littler et al., 2014; Zachos et al., 2010;
68 Sexton et al., 2011).

69 Several different carbon sources have been proposed to explain the negative CIE,
70 including: (1) the release of methane by thermal dissociation of gas hydrates on the
71 continental slopes (Dickens et al., 1995); (2) the burning of peat and coal deposits
72 (Kurtz et al., 2003); and (3) the release of carbon from thawing of permafrost soils at
73 high latitudes as a feedback or as a direct response to orbital forcing (DeConto et al.,
74 2012); while (4) a redistribution of ^{13}C -depleted carbon within oceans has been
75 proposed as mechanism for hyperthermals in the early to middle Eocene interval
76 (Sexton et al., 2011).

77 Despite the uncertainty in carbon source and triggering mechanism of the
78 hyperthermal events, a common reservoir has been theorized to explain the consistent
79 covariance in benthic foraminiferal $\delta^{13}\text{C}$ and $\delta^{18}\text{O}$ across both the PETM and ETM2,
80 indicating that changes in the exogenic carbon pool were similarly related to warming
81 during these events (Stap et al., 2010). The aim of this paper is to test this relationship
82 by constraining the relative timing and magnitude of changes in deep ocean
83 temperatures and carbon isotope excursions for a series of carbon isotope excursions
84 that succeed ETM2, initially identified by Cramer et al., (2003) in the composite bulk
85 carbonate $\delta^{13}\text{C}$ record from several deep-sea sites (ODP Sites 690 and 1051; DSDP
86 Site 550 and 577). For this purpose, we generated high-resolution carbon and oxygen
87 stable isotope records of the benthic foraminiferal species *Nuttalides truempyi* from
88 ODP Sites 1262 and 1263 (Walvis Ridge) encompassing the interval from the ETM2
89 (Stap et al., 2010) to the ETM3 (Röhl et al., 2005), providing the first complete high-
90 resolution benthic stable isotope records for the early Eocene events leading to the
91 onset of the EECO.

92

93 2 Materials and Methods

94 2.1 Site location and sampling

95 ODP Sites 1262 and 1263 represent the deepest and shallowest end-members of a 2-
96 km depth transect recovered during ODP Leg 208. Site 1263 is located just below the
97 crest of the northeast flank of Walvis Ridge, in the southeastern Atlantic, at a water
98 depth of 2717 m, whereas Site 1262 was drilled near the base of the northwestern
99 flank of Walvis Ridge at a water depth of 4759 m (Fig. 1). The estimated paleodepths
100 of Sites 1262 and 1263 at ~56 Ma were ~3600 m and 1500 m, respectively (Zachos et
101 al., 2004). The material recovered at the two sites provided an expanded sequence of
102 early Paleogene sediments, yielding a complete section mainly composed of
103 calcareous nannofossil ooze, chalk and marls. The composite depth scale for Site
104 1263 was constructed using the magnetic susceptibility (MS) and sediment lightness
105 (L^*) from the four holes (Zachos et al., 2004).

106 Samples were collected at the Bremen Core Repository from Holes A, B and C for
107 Site 1263, and Holes A and B for Site 1262, according to the shipboard meters
108 composite depth section (mcd) (Zachos et al., 2004). A 28-m thick interval of Site
109 1263 was sampled at a resolution of 5 cm from ~268 to ~296 mcd, and a ~6-m
110 interval of Site 1262 was sampled at a resolution of 3 cm from ~103 to ~109 mcd
111 (Fig. 3). Prior to the analyses, samples were freeze dried, washed and sieved to obtain
112 fractions larger than 38, 63 and 150 μm at University of California, Santa Cruz and
113 Utrecht University.

114

115 2.2 Stable isotopes

116 Multi-specimen samples of *N. truempyi* were picked from the >150 μm fraction. The
117 stable isotope values of picked specimens (average of 6–8 foraminiferal calcite tests)
118 from Site 1263 were carried out at Utrecht University using a CARBO-KIEL
119 automated carbonate preparation device linked on-line to a Thermo-Finnigan
120 MAT253 mass spectrometer. Calibrations to the international standard (NBS-19) and
121 to the in-house standard (Naxos marble) show an analytical precision of 0.03‰ and
122 0.08‰ for $\delta^{13}\text{C}$ and $\delta^{18}\text{O}$, respectively. The stable isotope values of picked specimens

123 from Site 1262 were analyzed on a KIEL IV carbonate preparation device linked on-
124 line to a Thermo-Finnigan MAT253 mass spectrometer, at the UCSC Stable Isotope
125 Laboratory, Santa Cruz. Calibrations to the in-house standard Carrara marble (CM05)
126 and international standards (NBS-18 and NBS-19) yield an analytical precision of
127 0.05‰ and 0.08‰, for $\delta^{13}\text{C}$ and $\delta^{18}\text{O}$, respectively. All values are reported in
128 standard delta notation relative to VPDB (Vienna Pee Dee Belemnite). Outliers were
129 defined by adding or subtracting an upper and lower boundary of 2σ from a 13-points
130 moving average, following the method by Liebrand et al. (2011). Published benthic
131 isotope data of the same foraminiferal species were included in this study to obtain
132 longer continuous records of Site 1263 and 1262 (Stap et al., 2010; Littler et al.,
133 2014), (Fig. 3 and 4).

134 **2.3 Paleotemperature reconstructions**

135 Paleotemperatures were obtained from the benthic foraminiferal $\delta^{18}\text{O}$ values by
136 applying the equation of Bemis et al. (1998):

$$137 \quad T (\text{°C}) = 16.9 - 4.38 (\delta^{18}\text{O}_c - \delta^{18}\text{O}_{\text{sw}}) + 0.10 (\delta^{18}\text{O}_c - \delta^{18}\text{O}_{\text{sw}})^2 \quad (1)$$

138 The temperature scale is computed assuming an ice-free sea water value ($\delta^{18}\text{O}_{\text{sw}}$) of -
139 1.2‰ (VPDB). This value is calculated correcting the estimated deep-sea $\delta^{18}\text{O}_{\text{sw}}$
140 value of -0.98‰ (SMOW) relative to PDB scales by subtracting 0.27‰ (Hut, 1987).
141 The *N. truempyi* $\delta^{18}\text{O}$ was adjusted for disequilibrium vital effects by adding 0.35‰
142 (Shackleton et al., 1984; Shackleton and Hall, 1997), on the assumption that the
143 isotopic disequilibrium for this species remained constant through time.

144

145 **3 Age model**

146 Given the typical low resolution age control afforded by magneto- and bio-
147 stratigraphy, and the availability of a robust cycle (i.e., orbital) based chronology for
148 the Leg 208 sites (Westerhold et al., 2007), we developed an eccentricity-tuned age
149 model for the studied interval using the red over green color ratio (a^*) records of ODP
150 Sites 1263 and 1262 (Fig. 2). For tuning, we applied first spectral analysis in the
151 depth domain using standard Blackman-Tukey and Gaussian filtering techniques as
152 provided by the AnalySeries program (Paillard et al., 1996). Site 1262, the deepest
153 site at Walvis Ridge, was chosen as the backbone for our tuning. The a^* record of this

154 site clearly revealed a ~3-m period, interpreted as reflecting the climatic imprint of the
155 405-kyr eccentricity cycle (Lourens et al., 2005). Subsequently, we filtered this
156 component and tuned it directly to the extracted 405-kyr eccentricity component of
157 the La2010d orbital solution (Laskar et al., 2011) with maximum a^* values,
158 interpreted to represent maximum carbonate dissolution, corresponding to maximum
159 eccentricity values (Table 1). A similar approach was carried out for the a^* record of
160 Site 1263 to evaluate the continuity of the successions and robustness of the filtered
161 output (Fig. 2). Finally, the tuned age model of Site 1262 was transferred to Site 1263
162 by correlating >50 characteristic features in the a^* records of both sites as tie points
163 (Fig. 2 and Table 2).

164 Different tuning options have been debated in the last 10 years, resulting in an age for
165 the PETM ranging between ~55.5 and ~56.3 Ma (Lourens et al., 2005; Westerhold et
166 al., 2008; Hilgen et al., 2010, Dinarès-Turell et al., 2014). Here we report on two
167 tuning options (Fig. 2), assigning an age of 53.69 ± 0.02 Ma (option 1) or of
168 54.09 ± 0.02 Ma (option 2) to ETM2 (Westerhold et al., 2007). According to both
169 options, ETM2 predates the 405-kyr maximum falling at an increasing limb, in
170 agreement with observations of Westerhold et al. (2007), but in contrast with the
171 earlier interpretation by Lourens et al. (2005), who aligned this event to a maximum
172 in the 405-kyr cycle. Recent literature revising the Paleocene cyclostratigraphic
173 interpretation (Dinarès-Turell et al., 2014; Hilgen et al., 2015) have shown that the
174 Paleocene holds 25, rather than 24, 405-kyr eccentricity cycles. In addition, new U/Pb
175 ages have become available which support an age of ~66.0 Ma for the K/Pg boundary
176 (Kuiper et al., 2008; Renne et al., 2013). These developments point to an age of ~54.0
177 Ma for ETM2 and therefore we plot our results anchoring the age of ETM2 to option
178 2 (Fig. 4). Evolutionary wavelet spectra were obtained in the time domain using the
179 wavelet script of Torrence and Compo (<http://paos.colorado.edu/research/wavelets>).
180 Prior to the analysis, carbon and oxygen records were resampled at 2.5 kyrs,
181 detrended and normalized.

182

183 **4 Results**

184 Our new benthic $\delta^{13}\text{C}$ and $\delta^{18}\text{O}$ records show six major negative excursions between
185 54 and 52 Ma (Fig. 4). They correspond to the ETM2, H2, I1, I2, J, and ETM3 (or
186 X/K) events, formerly recognized in deep-sea $\delta^{13}\text{C}$ bulk carbonate records and land-

187 based marine and continental sections (Abels et al., 2012; Agnini et al., 2009; Cramer
188 et al., 2003; Kirtland Turner et al., 2014; Littler et al., 2014; Lourens et al., 2005;
189 Slotnick et al., 2012; Abels et al., 2015).

190 The general long-term trend in our ~2-Myr long records indicates a minor increase
191 between 54.2 Ma and 53.2 Ma followed by an average decrease of ~0.3 ‰ in absolute
192 baseline values of both $\delta^{13}\text{C}$ and $\delta^{18}\text{O}$ following J (~53.1 Ma), accompanied by minor
193 cycles between the six main events in both records. Following J, both records
194 maintain rather stable values up to ETM3 (Fig. 4). These changes are negligible
195 compared to the Paleocene-Eocene long-term warming trend and long-term negative
196 trend in carbon isotope values. However, the onset of more generally negative $\delta^{13}\text{C}$
197 values, coinciding with J, has also been observed in the deep-sea bulk carbonate
198 record at Site 1262 (Zachos et al., 2010) and in the land-based section at Mead Stream
199 by Slotnick et al. (2012), who suggested that the pronounced change in lithology
200 beginning with J could be used as a chronostratigraphic marker for the onset of the
201 EECO.

202 Evidence for the onset of warmer temperatures leading to the EECO is evident at ~53
203 Ma in the benthic $\delta^{18}\text{O}$ records at both Sites 1262 and 1263 (Fig. 4). Baseline average
204 $\delta^{18}\text{O}$ values prior to ETM2, signifying the response of the unperturbed oceanic
205 system, indicate a mean deep-sea temperature of ~12°C, which post-J increases by
206 >0.5°C. Despite variability, our data shows that this increase in background
207 temperature continued upwards across ETM3. Here we suggest that the onset of the
208 EECO can be identified in our records with the onset of the general low in benthic
209 isotope values initiated with J (~53 Ma) and thus including ETM3 within the EECO.
210 Although longer high-resolution benthic $\delta^{18}\text{O}$ records are needed to establish the total
211 duration of the EECO, this could represent a first step towards a formal definition of
212 the warmest interval of the Cenozoic, avoiding ambiguity caused by changes in the
213 time scale.

214 On the short-term scale, our new data across the events following ETM2 and H2
215 indicate a rise in temperature of ~2 °C and ~1.5 °C during I1 and I2, respectively. The
216 J-event was associated with a temperature increase of >1°C superimposed on the
217 further average decrease in baseline $\delta^{18}\text{O}$ value. ETM3 is expressed in both the
218 shallowest and deepest site at Walvis Ridge by similar isotopic excursions, with a CIE

219 of $\sim 0.8\%$ and a negative shift in the $\delta^{18}\text{O}$ record of $\sim 0.5\%$, corresponding to a
220 warming in the deep ocean of $2\text{--}2.5^\circ\text{C}$, comparable to values observed during the
221 ETM2 (Stap et al., 2010).

222 Evolutionary wavelet analyses for $\delta^{13}\text{C}$ and $\delta^{18}\text{O}$ records of Site 1263 show spectral
223 power concentrated at distinct frequencies, corresponding to the long 405-kyr and
224 short $\sim 100\text{-kyr}$ eccentricity cycles (Fig. 5). The isotope records reveal coherent
225 patterns, with the highest spectral power concentrated during ETM2-H2 and I1-I2.
226 The $\sim 100\text{-kyr}$ signal in $\delta^{13}\text{C}$, which is very prominent in the first 1 Myr of the record,
227 weakens after J. The imprint of precession and/or obliquity forcing is very
228 weak/absent throughout the entire record. As a result of our tuning approach, minima
229 in $\delta^{13}\text{C}$ are approximately in phase with maxima in the 405-kyr and $\sim 100\text{-kyr}$
230 eccentricity cycles, following previous work (e.g., Cramer et al., 2003; Lourens et al.,
231 2005; Zachos et al., 2010; Stap et al., 2010).

232 **5 Discussion**

233 **5.1 Isotope covariance**

234 Our high-resolution benthic isotope records provide a direct constraint on the
235 relationship between the temperature-related signal carried by the benthic
236 foraminiferal $\delta^{18}\text{O}$ and the CIEs during the events leading to the EECO. The six
237 events recognised in the benthic records vary in terms of both magnitude of the CIEs
238 and inferred temperature changes. The most intense perturbations are associated with
239 ETM2, I1 and ETM3, whereas H2 and I2, which lag the larger events by one 100-kyr
240 eccentricity cycle, are less prominent (Fig. 4). One important question then is whether
241 all these events of varying magnitude are accompanied by the same source of light
242 carbon released into the ocean atmosphere system and climatic response. Following
243 Stap et al. (2010), we have assessed this by comparing the slopes of the regression
244 lines between the carbon and oxygen isotopes of the individual events (Fig. 6). These
245 cross-plots clearly show that all events exhibit significant and coherent linear
246 correlation at both sites with slopes ranging between 0.5 and 0.7 (Fig. 6), indicating a
247 consistent relationship for all events between changes in deep-sea temperatures and
248 carbon release. We conclude that this significant covariance between benthic $\delta^{13}\text{C}$ and
249 $\delta^{18}\text{O}$ records suggests a strong non-linear response to orbital forcing of global
250 temperatures and the release of isotopically light carbon (e.g. methane gas and/or

251 CO₂) into the ocean-atmosphere system during eccentricity maxima, driving
252 subsequent carbonate dissolution and enhanced greenhouse warming, as has been
253 observed in the older part of the record at Site 1262 (Stap et al., 2010; Littler et al.,
254 2014). This conclusion is further underlined by the consistent scaling of CIE
255 magnitudes between our deep-sea data and soil nodule records of the Bighorn basin
256 for these events, which strengthens the hypothesis of a similar isotopic composition of
257 the carbon source for the early Eocene hyperthermal events (Abels et al., 2015).

258

259 **5.2 The “paired” hyperthermal events**

260 The slopes of the regression lines for H2 and I2 appear slightly steeper than those of
261 ETM2, I1, J and ETM3 (Fig. 6). To statistically test this (dis)similarity, we applied a
262 Student t-test to pairs of slopes, comparing all the events against each other using both
263 a pooled and an unpooled error variance. The results show that the null hypothesis
264 (the slopes being similar, $\alpha=0.05$) is satisfied in the case of ETM2, I1, J and ETM3.
265 The tests on the steeper slopes of H2 and I2 generally display values of $p \leq 0.05$ when
266 tested against the other events, but values of $p \geq 0.05$ when tested against each other.
267 This implies that the smaller events, H2 and I2, are statistically similar to each other
268 but differ slightly from the other perturbations. Even though this statistical approach
269 might be subject to limitations derived from the range of data points chosen for each
270 event, it clearly shows that the slopes for H2 and I2 deviate from the average values
271 given by the other events. Moreover, the statistical deviation of the slopes of H2 and
272 I2 is clearer when comparing them with the average slope calculated for all the events
273 at each site, since the slopes of H2 and I2 fall outside the (99.99%) confidence limits
274 (Fig. 7). The average slope between $\delta^{13}\text{C}$ and $\delta^{18}\text{O}$ of 0.6 for both sites is also in
275 accord with previous observations for the onset/recovery of PETM, ETM2 and H2 by
276 Stap et al. (2010).

277 The “paired” hyperthermal events, ETM2-H2 and I1-I2 thus reveal slightly different
278 $\delta^{13}\text{C}$ vs. $\delta^{18}\text{O}$ relationships between their first (ETM2 and I1) and secondary (H2 and
279 I2) pulses. Assuming that these signals are globally representative, this could imply
280 that the second of the two pulses had a relatively larger contribution of an isotopically
281 heavier carbon source than the first pulse. Such a mechanism could hint to a methane-
282 related dominant carbon source (e.g. methane hydrates) during the initial phase of the
283 paired hyperthermal events that is mostly depleted, so that other relatively heavier

284 carbon isotope sources (e.g. wetlands, peat) become progressively more important
285 during the successive event. Warming of intermediate water during ETM2 and I1, as
286 previously suggested for the PETM and ETM2 (Jennions et al., 2015; Lunt et al.,
287 2010), could have destabilized methane clathrates leading to their dissociation and the
288 subsequent increased warming and large CIE. Mechanisms related to the depletion
289 and subsequent recharge time of the inferred methane clathrate reservoir between
290 ETM2 and H2, and I1 and I2, could explain why the second event had both a smaller
291 magnitude and possibly a smaller relative contribution of methanogenic carbon. The
292 smaller magnitude of the two secondary carbon pulses, regardless of the isotopic
293 composition of their source, seems feasible because the a^* values, interpreted as
294 representative of the degree of carbonate dissolution, were significantly lower than
295 during their preceding counterparts (Fig. 2). In other words, the degree of carbonate
296 dissolution associated with the shoaling of the calcite compensation depth (CCD) and
297 lysocline appears to be less severe than during the first pulses. In this respect it is
298 worth noting that H2 and I2 also behave differently from the “larger” events in terms
299 of biotic disruption. During PETM, ETM2 and I1, rates of variability in planktonic
300 communities indicate that the biotic response was proportional to the magnitude of
301 carbon injections, and biotic disruption linearly declined along with the decreasing
302 size of CIEs (Gibbs et al., 2012; Jennions et al., 2015). However, H2 and I2 do not
303 show evidence of above-background variance, suggesting that during these events the
304 system apparently failed to cross the environmental “threshold” necessary to generate
305 a detectable marine biotic disruption (D’haenens et al., 2012; Gibbs et al., 2012). This
306 all suggests that a change in the climate feedbacks and/or an incomplete recovery of
307 the buffering capacity of the ocean system after the first perturbation could have
308 played a significant role in amplifying the temperature response during the secondary
309 pulse. On the other hand, we cannot dismiss the possibility that local circulation
310 changes and/or partial dissolution slightly altered the anomalies in $\delta^{18}\text{O}$ and $\delta^{13}\text{C}$
311 during H2 and I2 at Walvis Ridge. Further research is hence needed to ratify the
312 (global) significance of this finding.

313

314 **5.3 Thresholds and orbital pacing**

315 The transition towards the EECO is marked by a general decrease of both benthic
316 carbon and oxygen isotopic values of $\sim 0.3\text{‰}$ at Site 1263, indicative of both long-

317 term warming and progressive oxidation of organic matter releasing CO₂ into the
318 ocean-atmosphere system. It has been theorized that the timing and magnitude of the
319 hyperthermals would respond to the crossing of a thermal threshold, more frequently
320 reached in phases of orbital-driven temperature increase (Lourens et al., 2005; Lunt et
321 al., 2011). In addition, the carbon reservoir or capacitor (Dickens, 2003), regardless of
322 its nature and as a result of the long-term temperature increase from the late
323 Paleocene to the early Eocene, would be largely depleted by the peak of the EECO,
324 leading to an interval free of hyperthermals. In turn, a series of orbitally paced global
325 warming events of decreasing frequency and increased size are expected to occur
326 during the post-EECO cooling phase when the carbon reservoir would have been
327 progressive refilled (e.g., Kirtland Turner et al., 2014). This hypothesis has been
328 questioned with data from a composite bulk stable isotope record of Site 1258
329 showing that a series of negative stable isotope excursions continued throughout the
330 EECO. This evidence suggests that episodes of carbon release persisted during the
331 peak of warmth and the onset of the cooling trend (Kirtland Turner et al., 2014).
332 Kirtland Turner and co-authors (2014) suggest that the mechanisms operating in the
333 early Eocene climate were not necessarily exceptional but actually similar to those
334 invoked for the Oligocene and Miocene when cyclic variations in the carbon cycle
335 were also clearly paced by orbital forcing, particularly in the eccentricity bands
336 (Holbourn et al., 2007; Pälike et al., 2006; Zachos et al., 2001b). Although the carbon
337 and oxygen isotope records of the Oligocene-Miocene and early Eocene are certainly
338 paced by eccentricity, their appearance in terms of punctuation are clearly different.
339 In particular, a relatively sudden release (storage) of large amounts of light carbon
340 (e.g. methane hydrates) into the ocean-atmosphere system seems the only way to
341 explain the unusual magnitude of the CIEs recorded at Walvis Ridge given the
342 rate/magnitude of warming, as well as carbonate dissolution and changes in benthic
343 assemblages associated with those events (Jennions et al., 2015; Stap et al., 2009).

344

345 **5.4 Site 1263 vs. Site 1262**

346 Comparison between the benthic $\delta^{13}\text{C}$ and $\delta^{18}\text{O}$ records of Sites 1263 and 1262
347 reveals an almost identical pattern, although $\delta^{18}\text{O}$ values of Site 1263 are consistently
348 $\sim 0.2\text{‰}$ heavier than those of Site 1262 (Fig. 3 and 4). A similar (reversed) pattern has
349 been previously observed by Stap et al. (2009) in the case of ETM2, and attributed to

350 differential dissolution from the shallowest to the deepest site. Conversely, selective
351 dissolution seems unlikely to justify the persistent offset in $\delta^{18}\text{O}$ values observed
352 throughout the new post-ETM2 record presented herein. We posit that this offset may
353 be linked to a different average isotopic composition of the water masses at those
354 sites. Accordingly, the intermediate water masses reaching Site 1263 were more ^{18}O -
355 enriched than the deeper waters at Site 1262. The existence of a discrete intermediate
356 water body in the early Eocene South Atlantic is supported by recent benthic
357 foraminiferal assemblage, sedimentological evidence and Earth system modeling data
358 across ETM2, which suggests that warming in the intermediate waters bathing Site
359 1263 led to differential patterns in sedimentary and ecological data between this site
360 and the deeper Site 1262 (Jennions et al., 2015).

361 **6 Conclusions**

362 New high-resolution benthic stable isotope records from ODP Sites 1262 and 1263
363 provide a detailed framework to explore the (transient) nature of early Eocene
364 hyperthermal events during the onset of the EECO. Our results further confirm the
365 link between large-scale carbon release and climate response to orbital forcing, in
366 particular to short- and long- eccentricity cycles. The transition towards the EECO is
367 marked by a general decrease of both benthic carbon and oxygen isotopic values of
368 $\sim 0.3\text{‰}$ at Site 1263, indicative of both long-term warming and progressive oxidation
369 of organic matter releasing CO_2 into the ocean-atmosphere system. Consistent
370 covariance between benthic carbon and oxygen isotopes demonstrates that global
371 temperatures and changes in the exogenic carbon pool were similarly coupled during
372 each of the studied hyperthermal events. In this regard, we found that the second
373 pulses of the paired hyperthermal events (i.e. H2 and I2) point to a slightly different
374 behavior. Whether this implies a larger role for a carbon reservoir characterized by a
375 heavier isotopic signature remains debatable and, hence, allows for further
376 consideration of other operational processes such as local circulation changes, partial
377 dissolution, or different climate feedbacks. Finally we found a constant offset in
378 oxygen isotopic values between Site 1263 and 1262, with the isotopic composition of
379 the shallower waters at Site 1263 consistently heavier than at Site 1262, suggesting
380 presence of a discrete water body at intermediate depths of the Walvis Ridge transect.

381 **Acknowledgements**

382 We are grateful to Gerald Dickens, Lee Kump and Philip Sexton for their constructive
383 comments. We thank the International Ocean Discovery Program (IODP) for
384 providing the samples used in this study. We also thank A. van Dijk at Utrecht
385 University, and Dyke Andreasen and Chih-Ting Hsieh at UCSC for analytical
386 support. This research was funded by NWO-ALW grant (project number 865.10.001)
387 to L.J. Lourens. We thank F. Hilgen and H.A. Abels for providing valuable comments
388 on the manuscript.

389 **References**

- 390 Abels, H. A., Clyde, W. C., Gingerich, P. D., Hilgen, F. J., Fricke, H. C., Bowen, G.
391 J. and Lourens, L. J.: Terrestrial carbon isotope excursions and biotic change during
392 Palaeogene hyperthermals, *Nat. Geosci.*, 5(5), 326–329, doi:10.1038/ngeo1427, 2012.
- 393 Abels, H. A., Lauretano, V., van Yperen, A., Hopman, T., Zachos, J. C., Lourens, L.
394 J., Gingerich, P. D., Bowen, G. J.: Carbon isotope excursions in paleosol carbonate
395 marking five early Eocene hyperthermals in the Bighorn Basin, Wyoming, *Clim. Past*
396 Discussion, <http://www.clim-past-discuss.net/11/1857/2015/cpd-11-1857-2015.html>.
- 397 Agnini, C., Macri, P., Backman, J., Brinkhuis, H., Fornaciari, E., Giusberti, L.,
398 Luciani, V., Rio, D., Sluijs, A. and Speranza, F.: An early Eocene carbon cycle
399 perturbation at ~52.5 Ma in the Southern Alps: Chronology and biotic response,
400 *Paleoceanography*, 24(2), doi:10.1029/2008PA001649, 2009.
- 401 Bemis, B. E., Spero, H. J., Bijma, J., and Lea, D. W.: Reevaluation of the oxygen
402 isotopic composition of planktonic foraminifera: Experimental results and revised
403 paleotemperature equations: *Paleoceanography*, v. 13, p. 150-160, 1998.
- 404 Bijl, P. K., Schouten, S., Sluijs, A., Reichart, G.-J., Zachos, J. C. and Brinkhuis, H.:
405 Early Palaeogene temperature evolution of the southwest Pacific Ocean., *Nature*,
406 461(7265), 776–9, doi:10.1038/nature08399, 2009.
- 407 Cramer, B. S., Wright, J. D., Kent, D. V and Aubry, M.-P.: Orbital climate forcing of
408 $\delta^{13}\text{C}$ excursions in the late Paleocene–early Eocene (chrons C24n–C25n),
409 *Paleoceanography*, 18(4), doi:10.1029/2003PA000909, 2003.
- 410 D’haenens, S., Bornemann, A., Stassen, P. and Speijer, R. P.: Multiple early Eocene
411 benthic foraminiferal assemblage and $\delta^{13}\text{C}$ fluctuations at DSDP Site 401 (Bay of
412 Biscay — NE Atlantic), *Mar. Micropaleontol.*, 88-89, 15–35,
413 doi:10.1016/j.marmicro.2012.02.006, 2012.
- 414 DeConto, R. M., Galeotti, S., Pagani, M., Tracy, D., Schaefer, K., Zhang, T., Pollard,
415 D. and Beerling, D. J.: Past extreme warming events linked to massive carbon release
416 from thawing permafrost., *Nature*, 484(7392), 87–91, doi:10.1038/nature10929, 2012.
- 417 Dickens, G. R.: Rethinking the global carbon cycle with a large, dynamic and
418 microbially mediated gas hydrate capacitor, *Earth Planet. Sci. Lett.*, 213(3-4), 169–
419 183, doi:10.1016/S0012-821X(03)00325-X, 2003.
- 420 Dickens, G.R, J.R. O’Neil, D.K. Rea, and R.M. Owen: Dissociation of oceanic
421 methane hydrate as a cause of the carbon isotope excursion at the end of the
422 Paleocene. *Paleoceanography* 10, 965-971, 1995.
- 423 Dinarès-Turell, J., Westerhold, T., Pujalte, V., Röhl, U. and Kroon, D.: Astronomical
424 calibration of the Danian stage (Early Paleocene) revisited: Settling chronologies of
425 sedimentary records across the Atlantic and Pacific Oceans, *Earth Planet. Sci. Lett.*,
426 405, 119–131, doi:10.1016/j.epsl.2014.08.027, 2014.

- 427 Galeotti, S., Krishnan, S., Pagani, M., Lanci, L., Gaudio, A., Zachos, J. C., Monechi,
428 S., Morelli, G. and Lourens, L. J.: Orbital chronology of Early Eocene hyperthermals
429 from the Contessa Road section, central Italy, *Earth Planet. Sci. Lett.*, 290(1-2), 192–
430 200, doi:10.1016/j.epsl.2009.12.021, 2010.
- 431 Gibbs, S. J., Bown, P. R., Murphy, B. H., Sluijs, A., Edgar, K. M., Pälike, H., Bolton,
432 C. T. and Zachos, J. C.: Scaled biotic disruption during early Eocene global warming
433 events, *Biogeosciences*, 9(11), 4679–4688, doi:10.5194/bg-9-4679-2012, 2012.
- 434 Hilgen, F. J., Abels, H. A., Kuiper, K. F., Lourens, L. J. and Wolthers, M.: Towards a
435 stable astronomical time scale for the Paleocene: Aligning Shatsky Rise with the
436 Zumaia – Walvis Ridge ODP Site 1262 composite, *Newsletters Stratigr.*, 48(1), 91–
437 110, doi:10.1127/nos/2014/0054, 2015.
- 438 Hilgen, F. J., Kuiper, K. F. and Lourens, L. J.: Evaluation of the astronomical time
439 scale for the Paleocene and earliest Eocene, *Earth Planet. Sci. Lett.*, 300(1-2), 139–
440 151, doi:10.1016/j.epsl.2010.09.044, 2010.
- 441 Holbourn, A., Kuhnt, W., Schulz, M., Flores, J-A. and Andersen, N.: Orbitally-paced
442 climate evolution during the middle Miocene “Monterey” carbon isotope excursion,
443 *Earth Planet. Sci. Lett.* 261, 534–550, 2007.
- 444 Hönisch, B., Ridgwell, A., Schmidt, D. N., Thomas, E., Gibbs, S. J., Sluijs, A., Zeebe,
445 R., Kump, L., Martindale, R. C., Greene, S. E., Kiessling, W., Ries, J., Zachos, J. C.,
446 Royer, D. L., Barker, S., Marchitto, T. M., Moyer, R., Pelejero, C., Ziveri, P., Foster,
447 G. L. and Williams, B.: The geological record of ocean acidification, *Science*,
448 335(6072), 1058–63, doi:10.1126/science.1208277, 2012.
- 449 Hut, G.: Consultants group meeting on stable isotope reference samples for
450 geochemical and hydrological investigations: Vienna, Austria, Report to Director
451 General of the Institute of Atomic Energy Agency, 42, 1987.
- 452 Jennions, S. M., Thomas, E., Schmidt, D. N., Lunt, D., and Ridgwell, A.: Changes in
453 benthic ecosystems and ocean circulation in the Southeast Atlantic across Eocene
454 Thermal Maximum 2, *Paleoceanography*, 30, doi:10.1002/2015PA002821, 2015.
- 455 Kennett, J. P. and Stott, L. D.: Abrupt deep-sea warming, palaeoceanographic
456 changes and benthic extinctions at the end of the Palaeocene, *Nature*, 353(6341), 225–
457 229, doi:10.1038/353225a0, 1991.
- 458 Kirtland Turner, S., Sexton, P. F., Charles, C. D. and Norris, R. D.: Persistence of
459 carbon release events through the peak of early Eocene global warmth, *Nat. Geosci.*,
460 12(9), 1–17, doi:10.1038/ngeo2240, 2014.
- 461 Kuiper, K. F., Deino, a, Hilgen, F. J., Krijgsman, W., Renne, P. R. and Wijbrans, J.
462 R.: Synchronizing rock clocks of Earth history., *Science*, 320(5875), 500–4,
463 doi:10.1126/science.1154339, 2008.

- 464 Kurtz, A. C., Kump, L. R., Arthur, M. A., Zachos, J. C. and Paytan, A.: Early
465 Cenozoic decoupling of the global carbon and sulfur cycles, *Paleoceanography*, 18(4),
466 doi:10.1029/2003PA000908, 2003.
- 467 Laskar, J., Fienga, A., Gastineau, M., and Manche, H.: La2010: A new orbital
468 solution for the long term motion of the Earth: *Astron. Astrophys.*, Volume 532, A89,
469 2011.
- 470 Liebrand, D., Lourens, L. J., Hodell, D. A., De Boer, B., Van De Wal, R. S. W. and
471 Pälike, H.: Antarctic ice sheet and oceanographic response to eccentricity forcing
472 during the early Miocene, *Clim. Past*, 7(3), 869–880, doi:10.5194/cp-7-869-2011,
473 2011.
- 474 Littler, K., Röhl, U., Westerhold, T. and Zachos, J. C.: A high-resolution benthic
475 stable-isotope record for the South Atlantic: Implications for orbital-scale changes in
476 Late Paleocene-Early Eocene climate and carbon cycling, *Earth Planet. Sci. Lett.*,
477 401, 18–30, doi:10.1016/j.epsl.2014.05.054, 2014.
- 478 Lourens, L. J., Sluijs, A., Kroon, D., Zachos, J. C., Thomas, E., Röhl, U., Bowles, J.
479 and Raffi, I.: Astronomical pacing of late Palaeocene to early Eocene global warming
480 events., *Nature*, 435(7045), 1083–1087, doi:10.1038/nature03814, 2005.
- 481 Lunt, D. J., Valdes, P. J., Jones, T. D., Ridgwell, A., Haywood, A. M., Schmidt, D.
482 N., Marsh, R. and Maslin, M.: CO₂-driven ocean circulation changes as an amplifier
483 of Paleocene-Eocene thermal maximum hydrate destabilization, *Geology*, 38(10),
484 875–878, doi:10.1130/G31184.1, 2010.
- 485 Lunt, D. J., Ridgwell, A., Sluijs, A., Zachos, J. C., Hunter, S. and Haywood, A.: A
486 model for orbital pacing of methane hydrate destabilization during the Palaeogene,
487 *Nat. Geosci.*, 4(11), 775–778, doi:10.1038/ngeo1266, 2011.
- 488 McInerney, F. A. and Wing, S. L.: The Paleocene-Eocene Thermal Maximum: A
489 Perturbation of Carbon Cycle, Climate, and Biosphere with Implications for the
490 Future, *Annu. Rev. Earth Planet. Sci.*, 39(1), 489–516, doi:10.1146/annurev-earth-
491 040610-133431, 2011.
- 492 Nicolo, M. J., Dickens, G. R., Hollis, C. J. and Zachos, J. C.: Multiple early Eocene
493 hyperthermals: Their sedimentary expression on the New Zealand continental margin
494 and in the deep sea, *Geology*, 35(8), 699, doi:10.1130/G23648A.1, 2007.
- 495 Paillard, D., Labeyrie, L., Yiou, P.: Macintosh program performs time-series analysis.
496 *Eos Trans. AGU* 77, 379, 1996.
- 497 Pälike, H., Norris, R. D., Herrle, J. O., Wilson, P. A., Coxall, H. K., Lear, C. H.,
498 Shackleton, N.J., Tripathi, A.K., Wade, B.S.: The heart-beat of the Oligocene climate
499 system, *Science* 314, 1894–1998, 2006.
- 500 Renne, P. R., Deino, A. L., Hilgen, F. J., Kuiper, K. F., Mark, D. F., Mitchell, W. S.,
501 Morgan, L. E., Mundil, R. and Smit, J.: Time scales of critical events around the

- 502 Cretaceous-Paleogene boundary, *Science*, 339(6120), 684–7,
503 doi:10.1126/science.1230492, 2013.
- 504 Röhl, U., Westerhold, T., Monechi, S., Thomas, E., Zachos, J. C., Donner, B., 2005.
505 The Third and Final Early Eocene Thermal Maximum: Characteristics, Timing and
506 Mechanisms of the ‘X’ Event, GSA Annual Meeting 37. Geological Society of
507 America, Salt Lake City, USA. 264 pp
- 508 Sexton, P. F., Norris, R. D., Wilson, P. A., Pälike, H., Westerhold, T., Röhl, U.,
509 Bolton, C. T. and Gibbs, S.: Eocene global warming events driven by ventilation of
510 oceanic dissolved organic carbon, *Nature*, 471(7338), 349–352,
511 doi:10.1038/nature09826, 2011.
- 512 Shackleton, N. J., M. A. Hall, and A. Boersma: Oxygen and carbon isotope data from
513 Leg-74 foraminifers, Initial Rep. Deep Sea Drill. Project, 74, 599–612, 1984.
- 514 Shackleton, N. J., and Hall, M. A: The late Miocene stable isotope record, Site 926,
515 Proc. Ocean Drill. Program Sci. Results, 154, 367–373. doi:
516 10.2973/odp.proc.sr.154.119.1997
- 517 Slotnick, B. S., Dickens, G. R., Nicolo, M. J., Hollis, C. J., Crampton, J. S., Zachos, J.
518 C. and Sluijs, A.: Large-Amplitude Variations in Carbon Cycling and Terrestrial
519 Weathering during the Latest Paleocene and Earliest Eocene: The Record at Mead
520 Stream, New Zealand, *J. Geol.*, 120(5), 487–505, doi:10.1086/666743, 2012.
- 521 Sluijs, A., Brinkhuis, H., Schouten, S., Bohaty, S. M., John, C. M., Zachos, J. C.,
522 Reichart, G.-J., Sinninghe Damsté, J. S., Crouch, E. M. and Dickens, G. R.:
523 Environmental precursors to rapid light carbon injection at the Palaeocene/Eocene
524 boundary., *Nature*, 450(7173), 1218–21, doi:10.1038/nature06400, 2007.
- 525 Stap, L., Lourens, L. J., Thomas, E., Sluijs, A., Bohaty, S. and Zachos, J. C.: High-
526 resolution deep-sea carbon and oxygen isotope records of Eocene Thermal Maximum
527 2 and H2, *Geology*, 38(7), 607–610, doi:10.1130/G30777.1, 2010.
- 528 Stap, L., Sluijs, A., Thomas, E. and Lourens, L. J.: Patterns and magnitude of deep
529 sea carbonate dissolution during Eocene Thermal Maximum 2 and H2, Walvis Ridge,
530 southeastern Atlantic Ocean, *Paleoceanography*, 24(1), doi:10.1029/2008PA001655,
531 2009.
- 532 Thomas, E. and Shackleton, N. J.: The Paleocene-Eocene benthic foraminiferal
533 extinction and stable isotope anomalies, *Geol. Soc. London, Spec. Publ.*, 101(1), 401–
534 441, doi:10.1144/GSL.SP.1996.101.01.20, 1996.
- 535 Westerhold, T. and Röhl, U.: High resolution cyclostratigraphy of the early Eocene –
536 new insights into the origin of the Cenozoic cooling trend, *Clim. Past Discuss.*, 5(1),
537 495–534, 2009.
- 538 Westerhold, T., Röhl, U., Laskar, J., Raffi, I., Bowles, J., Lourens, L. J. and Zachos, J.
539 C.: On the duration of magnetochrons C24r and C25n and the timing of early Eocene
540 global warming events: Implications from the Ocean Drilling Program Leg 208

- 541 Walvis Ridge depth transect, *Paleoceanography*, 22(2), doi:10.1029/2006PA001322,
542 2007.
- 543 Westerhold, T., Röhl, U., Raffi, I., Fornaciari, E., Monechi, S., Reale, V., Bowles, J.
544 and Evans, H. F.: Astronomical calibration of the Paleocene time, *Palaeogeogr.*
545 *Palaeoclimatol. Palaeoecol.*, 257(4), 377–403, doi:10.1016/j.palaeo.2007.09.016,
546 2008.
- 547 Zachos, J. C., Pagani, M., Sloan, L., Thomas, E. and Billups, K.: Trends, rhythms,
548 and aberrations in global climate 65 Ma to present., *Science*, 292(5517), 686–693,
549 2001a.
- 550 Zachos, J. C., Shackleton, N. J., Revenaugh, J. S., Pälike, H., and Flower, B. P.,
551 Periodic and non-periodic climate response to orbital forcing across the Oligocene-
552 Miocene boundary. *Science*. 292, 274-277, 2001b
- 553 Zachos, J. C., Kroon, D. and Blum, P.: ODP Leg 208: The early Cenozoic extreme
554 climates transect along Walvis Ridge, *Proceedings of the Ocean Drilling Program*
555 *Initial Reports*, 208, 2004.
- 556 Zachos, J. C., Röhl, U., Schellenberg, S. A., Sluijs, A., Hodell, D. A., Kelly, D. C.,
557 Thomas, E., Nicolo, M., Raffi, I., Lourens, L. J., McCarren, H., and Kroon, D.: Rapid
558 acidification of the ocean during the Paleocene-Eocene thermal maximum.: *Science*
559 (New York, N.Y.), v. 308, no. 5728, p. 1611–5, doi: 10.1126/science.1109004, 2005.
- 560 Zachos, J. C., Dickens, G. R. and Zeebe, R. E.: An early Cenozoic perspective on
561 greenhouse warming and carbon-cycle dynamics., *Nature*, 451(7176), 279–283,
562 doi:10.1038/nature06588, 2008.
- 563 Zachos, J. C., McCarren, H., Murphy, B., Röhl, U. and Westerhold, T.: Tempo and
564 scale of late Paleocene and early Eocene carbon isotope cycles: Implications for the
565 origin of hyperthermals, *Earth Planet. Sci. Lett.*, 299(1-2), 242–249,
566 doi:10.1016/j.epsl.2010.09.004, 2010.
- 567 Zeebe, R. E. and Zachos, J. C.: Long-term legacy of massive carbon input to the Earth
568 system: Anthropocene versus Eocene., *Philos. Trans. A. Math. Phys. Eng. Sci.*,
569 371(2001), 2013.
- 570

571 TABLE 1: Age-depth tie points based on the tuning of the filtered 3-m period extracted from
 572 the color reflectance record of Site 1262 and the long-eccentricity cycle extracted from the
 573 Laskar solution La2010d (Laskar et al., 2011).

574

Site 1262 3-m period filter	Long-eccentricity cycle (kyrs)	
	<i>Laskar 2010d</i>	<i>Laskar 2010d</i>
	(Option 1)	(Option 2)
102.750	51800	52206
104.231	52003	52410
105.711	52206	52614
107.167	52410	52816
108.648	52614	53017
110.129	52816	53216
111.635	53017	53415
113.193	53216	53615
114.750	53415	53815
116.359	53615	54016
117.865	53815	54218

575

576 TABLE 2: Tie points between ODP Site 1263 and Site 1262 based on color reflectance
 577 records and interpolated ages obtained from the astronomically tuned age model.

Samples	Site 1263 Depth (mbsf)	Site 1263 Depth (mcd)	Samples	Site 1262 Depth (mbsf)	Site 1262 Depth (mcd)	Interpolated Age (Ma)	
						Option 1	Option 2
1263A-26H-4, 147.5	228.575	265.425	1262B-11H-4, 137.5	92.275	101.855	51.610	52.014
1263A-26H-5, 50	229.1	265.95	1262B-11H-5, 42.5	92.825	102.405	51.727	52.132
1263A-26H-5, 90	229.5	266.35	1262B-11H-5, 102.5	93.425	103.005	51.835	52.241
1263A-26H-5, 115	229.75	266.6	1262B-11H-5, 137.5	93.775	103.355	51.883	52.289
1263A-26H-6, 147.5	231.575	268.425	1262B-11H-6, 45	94.35	103.93	51.962	52.369
1263A-26H-7, 30	231.9	268.75	1262A-10H-2, 120	88.2	104.31	52.014	52.421
1263B-22H-5, 100	230.9	269.23	1262A-10H-2, 145	88.45	104.56	52.048	52.455
1263B-22H-5, 125	231.15	269.48	1262A-10H-3, 20	88.7	104.81	52.082	52.490
1263B-22H-6, 142.5	232.825	271.155	1262A-10H-3, 60	89.1	105.21	52.137	52.545
1263B-22H-7, 45	233.35	271.68	1262A-10H-3, 87.5	89.375	105.485	52.175	52.583
1263A-27H-1, 65	232.75	272.78	1262A-10H-4, 2.5	90.025	106.135	52.265	52.673
1263A-27H-2, 7.5	233.675	273.705	1262A-10H-4, 27.5	90.275	106.385	52.300	52.707
1263A-27H-2, 17.5	233.775	273.805	1262A-10H-4, 37.5	90.375	106.485	52.314	52.721
1263A-27H-2, 25	233.85	273.88	1262A-10H-4, 45	90.45	106.56	52.325	52.732
1263A-27H-2, 125	234.85	274.88	1262A-10H-4, 77.5	90.775	106.885	52.370	52.777
1263A-27H-2, 145	235.05	275.08	1262B-12H-1, 70	96.6	107.24	52.420	52.826
1263A-27H-3, 40	235.5	275.53	1262B-12H-1, 85	96.75	107.39	52.441	52.846
1263A-27H-3, 67.5	235.775	275.805	1262B-12H-1, 100	96.9	107.54	52.461	52.867
1263A-27H-3, 100	236.1	276.13	1262B-12H-1, 110	97	107.64	52.475	52.880
1263A-27H-3, 135	236.45	276.48	1262B-12H-1, 120	97.1	107.74	52.489	52.894
1263A-27H-4, 77.5	237.375	277.405	1262B-12H-2, 5	97.45	108.09	52.537	52.941
1263A-27H-4, 100	237.6	277.63	1262B-12H-2, 22.5	97.625	108.265	52.561	52.965
1263A-27H-4, 137.5	237.975	278.005	1262B-12H-2, 60	98	108.64	52.613	53.016
1263A-27H-5, 70	238.8	278.83	1262B-12H-2, 110	98.5	109.14	52.681	53.083
1263C-9H-4, 105	240.45	280.24	1262B-12H-2, 135	98.75	109.39	52.715	53.117
1263C-9H-5, 15	241.05	280.84	1262B-12H-3, 12.5	99.025	109.665	52.753	53.154
1263C-9H-5, 100	241.9	281.69	1262B-12H-3, 40	99.3	109.94	52.790	53.191
1263C-9H-6, 2.5	242.425	282.215	1262B-12H-3, 57.5	99.475	110.115	52.814	53.214
1263C-9H-6, 15	242.55	282.34	1262B-12H-3, 65	99.55	110.19	52.824	53.224
1263C-9H-6, 32.5	242.725	282.515	1262B-12H-3, 85	99.75	110.39	52.851	53.251
1263C-9H-6, 82.5	243.225	283.015	1262B-12H-4, 10	100.5	111.14	52.951	53.350
1263A-28H-1, 40	242	284.52	1262B-12H-4, 65	101.05	111.69	53.024	53.422
1263A-28H-1, 95	242.55	285.07	1262B-12H-4, 122.5	101.625	112.265	53.097	53.496
1263A-28H-1, 115	242.75	285.27	1262A-11H-1, 137.5	96.375	112.425	53.118	53.516
1263A-28H-2, 40	243.5	286.02	1262A-11H-2, 2.5	96.525	112.575	53.137	53.536
1263A-28H-2, 70	243.8	286.32	1262A-11H-2, 12.5	96.625	112.675	53.150	53.549
1263A-28H-2, 107.5	244.175	286.695	1262A-11H-2, 50	97	113.05	53.198	53.597
1263A-28H-3, 5	244.65	287.17	1262A-11H-2, 67.5	97.175	113.225	53.220	53.619
1263A-28H-3, 27.5	244.875	287.395	1262A-11H-2, 80	97.3	113.35	53.236	53.635
1263A-28H-3, 32.5	244.925	287.445	1262A-11H-2, 85	97.35	113.4	53.243	53.642

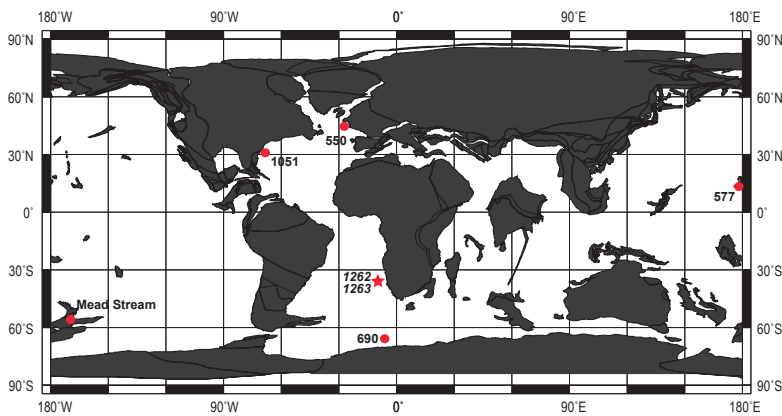
1263A-28H-3, 65	245.25	287.77	1262A-11H-2, 97.5	97.475	113.525	53.258	53.658
1263A-28H-3, 70	245.3	287.82	1262A-11H-2, 105	97.55	113.6	53.268	53.667
1263B-24H-2, 147.5	245.875	288.165	1262A-11H-2, 132.5	97.825	113.875	53.303	53.703
1263B-24H-3, 67.5	246.575	288.865	1262A-11H-2, 147.5	97.975	114.025	53.322	53.722
1263B-24H-4, 135	248.75	291.04	1262A-11H-3, 95	98.95	115	53.446	53.846
1263B-24H-5, 47.5	249.375	291.665	1262A-11H-3, 145	99.45	115.5	53.508	53.909
1263B-24H-6, 20	250.6	292.89	1262A-11H-4, 52.5	100.025	116.075	53.580	53.981
1263C-10H-5, 65	251.05	292.93	1262A-11H-4, 57.5	100.075	116.125	53.586	53.987
1263C-10H-5, 82.5	251.225	293.105	1262A-11H-4, 72.5	100.225	116.275	53.605	54.006
1263C-10H-5, 110	251.5	293.38	1262A-11H-4, 87.5	100.375	116.425	53.624	54.025
1263C-10H-7, 1	252.91	294.79	1262A-11H-4, 135	100.85	116.9	53.687	54.089
1263C-10H-7, 5	252.95	294.83	1262A-11H-5, 5	101.05	117.1	53.713	54.089
1263C-10H-7, 10	253	294.88	1262A-11H-5, 10	101.1	117.15	53.720	54.122

578

579 **FIGURES**

580 **Figure 1:** Paleogeographic reconstruction for the early Eocene (~54 Ma) showing the
581 position of Sites 1263 and 1262 (Walvis Ridge), (map provided by Ocean Drilling
582 Stratigraphic Network, ODSN;
583 <http://www.odsn.de/odsn/services/paleomap/paleomap.html>, modified). Also shown
584 the locations of ODP Sites 690 and 1051 and DSDP Sites 550 and 577 (Cramer et al.,
585 2003) and Mead Stream (Slotnick et al., 2012).

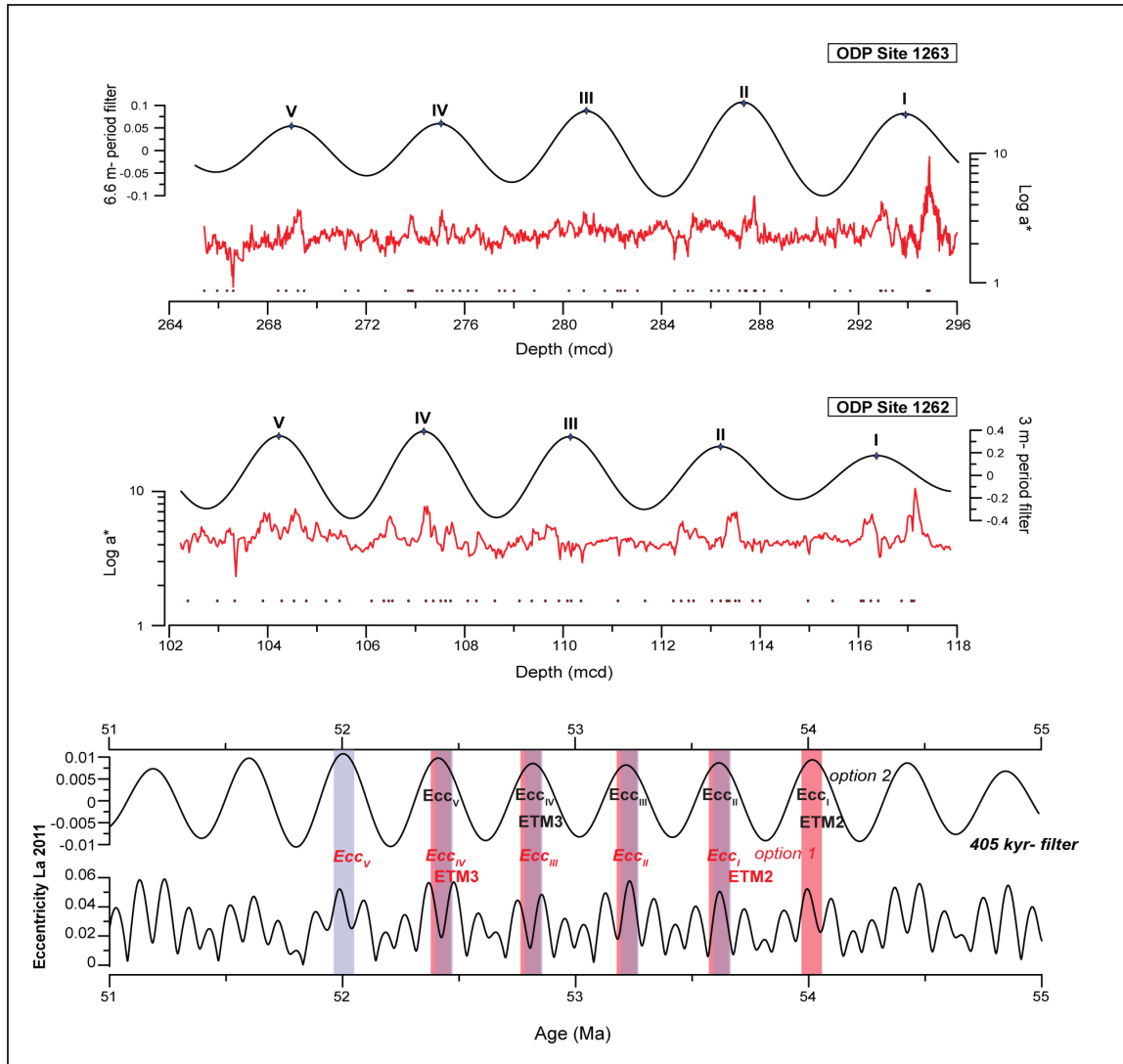
586



587

588

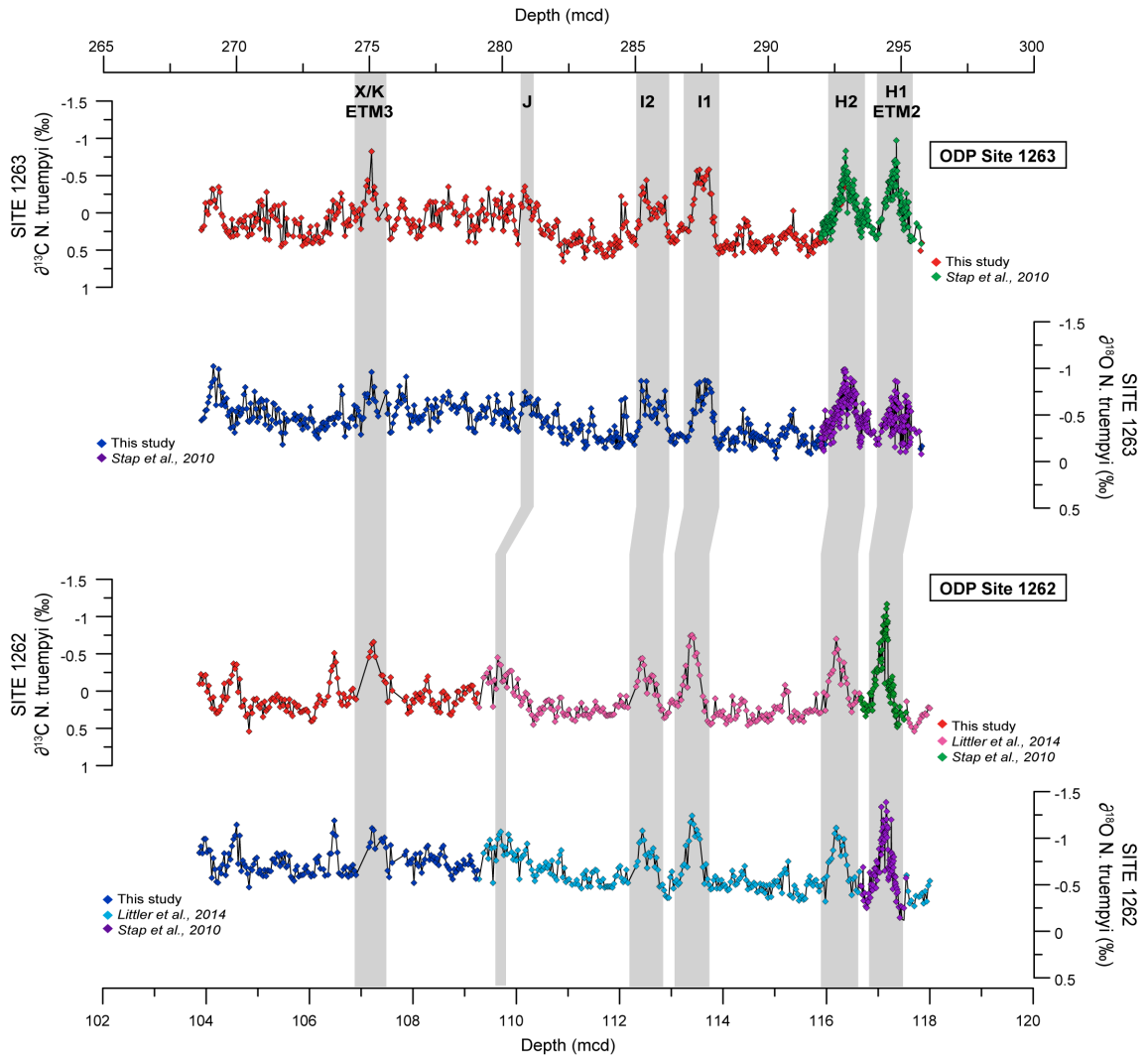
589 **Figure 2:** Floating orbitally tuned age model constructed using the red over green
 590 color ratio (a^*) record of ODP Sites 1262 (red line) and transferred to Site 1263 by
 591 using age-depth tie points between the sites (black dots, see Table 2). Two different
 592 tuning options are shown based on the ages proposed for the PETM by Westerhold et
 593 al. (2008).



594

595

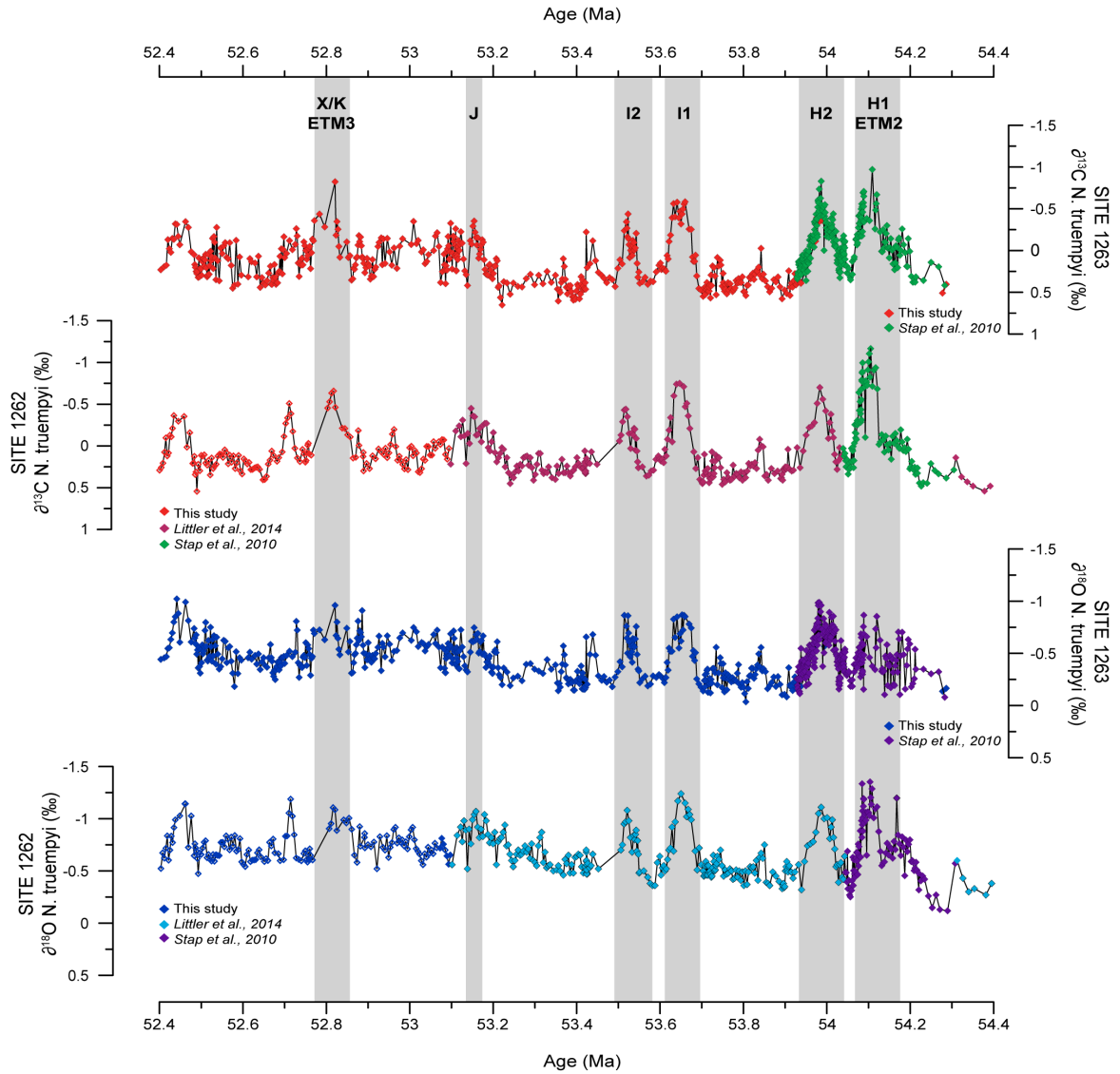
596 **Figure 3:** Benthic *N. truempyi* $\delta^{13}\text{C}$ and $\delta^{18}\text{O}$ records from Site 1263 and Site 1262,
 597 plotted versus depth. Highlighted intervals represent the position of the early Eocene
 598 hyperthermal events.



599

600

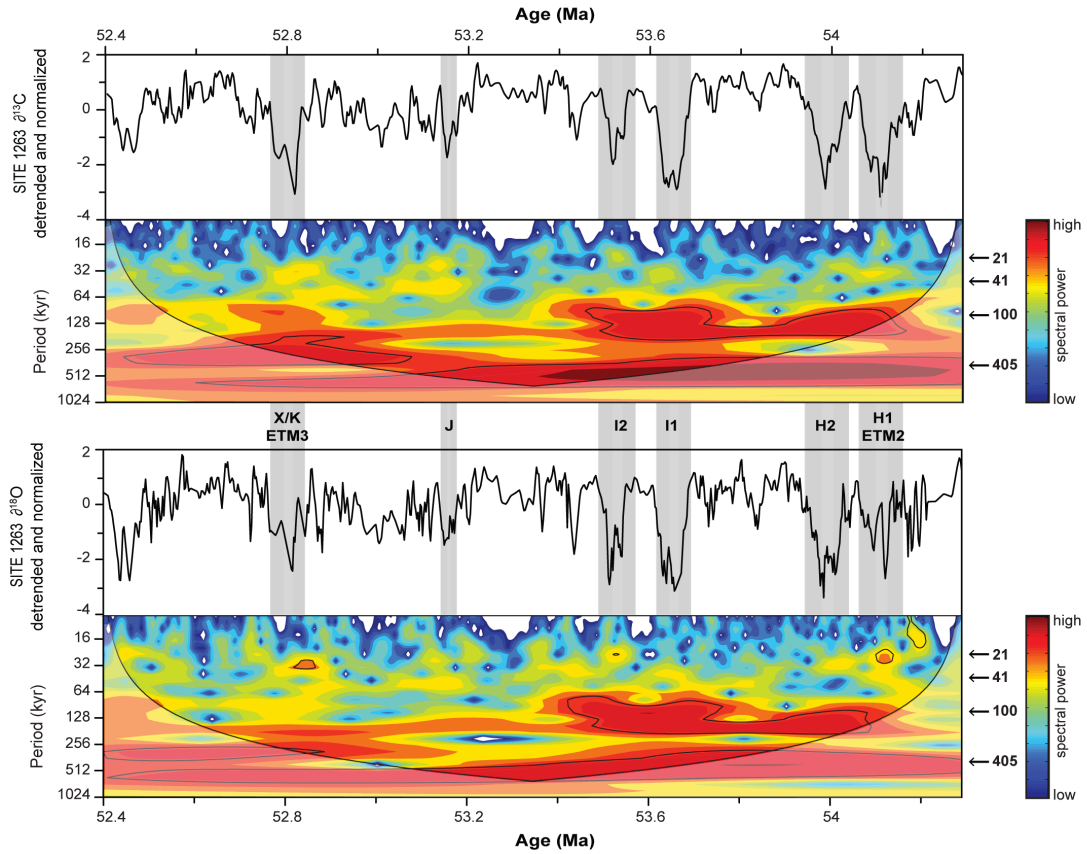
601 **Figure 4:** Benthic *N. truempyi* $\delta^{13}\text{C}$ and $\delta^{18}\text{O}$ records from Site 1263 and Site 1262,
 602 plotted versus Age (Ma), (starting from option 2 for the age of ETM2 by Westerhold
 603 et al., 2008). Highlighted intervals represent the position of the early Eocene
 604 hyperthermal events.



605

606

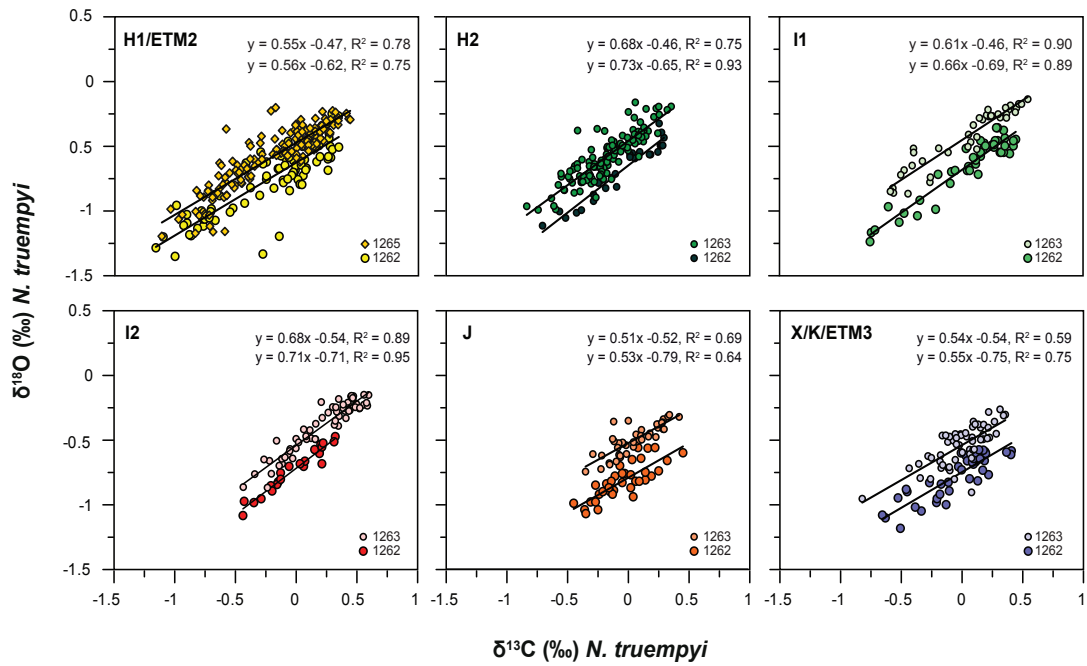
607 **Figure 5:** Evolutionary wavelet analyses for $\delta^{13}\text{C}$ and $\delta^{18}\text{O}$ were performed using a
608 Morlet mother wavelet of an order of 6. Shaded areas represent 95% significance
609 levels. Spectral power above the confidence level is concentrated at distinct
610 frequencies, corresponding to the long 405-kyr and short eccentricity 100-kyr cycles.
611 Highlighted intervals represent the position of the early Eocene hyperthermal events.



612

613

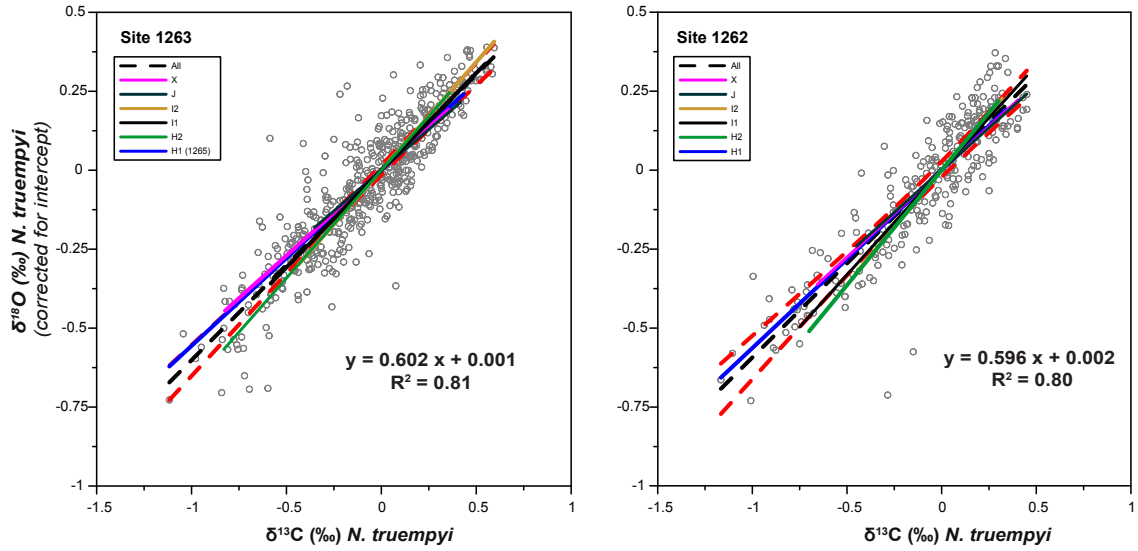
614 **Figure 6:** Relationship between the oxygen and carbon isotope values of *N. truempyi*
 615 during ETM2, H2, I1, I2, J and ETM3/X at Site 1263 and Site 1262. Note that,
 616 because of intense dissolution at Site 1263, ETM2 data were chosen from Site 1265
 617 (Stap et al., 2010). For all the events, throughout the entire event (onset+recovery
 618 phases), changes in the exogenic carbon pool are linearly related to warming. Linear
 619 regression equations refer to Site 1263 (top) and Site 1262 (bottom), respectively.



620

621

622 **Figure 7:** Regression line between $\delta^{13}\text{C}$ and $\delta^{18}\text{O}$ for each event plotted together with
623 the average slope (from all the events) at each site. The red dashed line indicates the
624 99% confidence interval.



625